Model Predictive Control of Wireless Power Transfer System in Seawater Environment

Ziyi Xia, *Student Member, IEEE*, Xin Dai, *Member, IEEE*, Yanling Li, Liuping Wang, *Senior Member, IEEE*, Fengwei Chen, *Member, IEEE*, and Wei Wang, *Student Member, IEEE*

***Abstract*—Wireless power transfer (WPT)systems have received more and more attention in undersea applications in recent years. The seawater between the transmitter and the receiver is a highly-conductive medium, which can be regarded as an unknown topology that will introduce eddy current loss and unknown dynamic behavior during the power transfer process. Hence, the dynamic modeling and control design methods for WPT systems in air may not apply. In this article, we propose an observer-free model predictive control (MPC) strategy for WPT systems in seawater environment. Considering the unknown topology introduced by the seawater medium, the control system is designed using a data-driven dynamic model obtained by simplified refined instrumental variable (SRIV) method. In a further step, the SRIV-based dynamic model is converted to a special state-space model by choosing a set of state variables corresponding to the input and output variables. Thus, the state observer design is avoided. Besides, operational constraints are imposed into the MPC algorithm to guarantee that the control input is implemented in an appropriate range. Experiments are performed to demonstrate that the proposed MPC system has superior performance in both reference tracking and parametric robustness in comparison to a proportional–integral control system.**

***Index Terms*—Data-driven modeling, model predictive control (MPC), operational constraints, seawater environment, simplified refined instrumental variable (SRIV), wireless power transfer (WPT).**

I. Introduction

WIRELESS power transfer (WPT) technique has been experiencing fast expanding in the market of mobile devices and electric vehicles [1], [2], [3], [4]. In recent years, WPT presents more and more importance in distributed ocean systems that consume a lot of electricity persistently [5], such as underwater robotics, ocean monitoring devices, and so on. It is time-consuming and costly to recharge or replace these devices manually, resulting in low efficiency as the ocean systems perform their tasks.

Although some researchers proposed to build undersea docking stations with electrical connectors for power supply [6], [7], [8], this solution suffers from high maintenance costs and limits to near-shore applications. Hence, considering the contactless transmission feature, it is reasonable to adopt WPT to recharge distributed ocean systems, which will be more convenient, flexible, and reliable. However, transferring power wirelessly in a marine environment, where seawater is a conducting medium, is still an open and challenging problem [9]. Besides, it should also be noted that in the area of biomedical engineering, WPT has many transcutaneous applications, for instance, replacing the skin-piercing wiring for powering implantable biomedical devices to avoid the discomfort and infection risks of patients [10], [11], [12]. Both areas share the same characteristics that the power transfer medium is nonair and conductive.

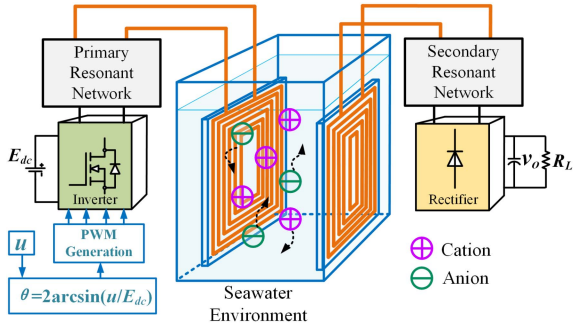

Fig. 1. Phase-shift regulated WPT System in seawater environment.

Fig. 1 shows a typical schematic diagram of the WPT system regulated by adjusting the phase shift of the inverter on the primary side, where the gap between the transmitter and receiver is filled with conductive liquid to simulate the seawater. As the transmitter constructs a high-frequency magnetic field across the medium, the induced electric field will drive the metal ions (including cations and anions) in the liquid to move and form clusters, effectively influencing the power transfer process. To better apply the WPT technique in real applications with conductive medium, it is expected that the system is stable and provides a fast dynamic response to both reference tracking and parametric variations.

Manuscript received 2 February 2024; revised 22 April 2024 and 20 June 2024; accepted 28 July 2024. Date of publication 6 August 2024; date of current version 7 October 2024. This work was supported by the research funds for the National Natural Science Foundation of China under Grant 51977178. Recommended for publication by Associate Editor J. Biela. *(Corresponding author: Xin Dai.)*

Ziyi Xia, Xin Dai, Fengwei Chen, and Wei Wang are with the College of Automation, Chongqing University, Chongqing 400044, China (e-mail: 20211301020@stu.cqu.edu.cn; daixin@cqu.edu.cn; fengwei.chen@cqu.edu.cn; 20173909@cqu.edu.cn).

Yanling Li is with the School of Electrical Engineering and Electronic Information, Xihua University, Chengdu 610039, China (e-mail: yanling.li@mail.xhu.edu.cn).

Liuping Wang is with the School of Engineering, Royal Melbourne Institute of Technology (RMIT), Melbourne, VIC 3000, Australia (e-mail: liuping.wang@rmit.edu.au).

Color versions of one or more figures in this article are available at https://doi.org/10.1109/TPEL.2024.3439331.

Digital Object Identifier 10.1109/TPEL.2024.3439331

In terms of control design for the WPT system with conductive medium, the following two questions remain to be addressed.

1) Since the seawater medium is considered, unknown numbers of parasitic resistors, capacitors and inductors are introduced. They will cause unknown nonlinear dynamics for the WPT system, making the conventional dynamic modeling methods less accurate because the parasitic parameters are often ignored. As a result, the controllers designed based on these models are no longer optimal.
2) The WPT system in air medium is always with high order and strong-nonlinearity. The introduced conductive medium will make the system much more complicated to analyze and so the controller design becomes more challenging.

For the modeling of the WPT system with seawater medium, many researchers concentrate on the steady-state description and the loss analysis. Zhou et al. [13] proposed a single-turn model of a circular coil with a ferrite core to calculate the eddy current loss (ECL) of the WPT system. Kim et al. [14] proposed an efficient modeling method for the WPT system using Z-parameters. In their research, by utilizing the electromagnetic analysis and two port network analysis, an impedance model of coils considering the frequency and the conductivity of seawater is derived. Yan et al. [15] proposed an analytic model of the ECL of a coreless WPT system in the seawater with Maxwell's equations, in which the expressions of the electric field intensity and the ECL are derived. Zhang et al. [16] proposed a modified mutual inductance circuit model for the WPT system to analyze the ECL and the detuning effect caused by the seawater. For the modeling of the WPT systems in biological tissues, Soltani et al. [17] used a lumped-element model to describe a 2-coil WPT system for implantable medical devices, where the specific absorption rate constraints in the tissue are embedded by using quasi-static field approximations. Oosterhout et al. [18] presented an analytical model based on the quasi-static approximation as a fast, yet sufficiently accurate tool for optimizing inductive charging systems of biomedical implants. Till now, the dynamic modeling methods for the WPT systems with conductive medium have not been reported yet.

For the control design of the WPT system, the related research is mainly focused on applications in air medium. Li et al. [19] proposed an H_∞ controller using the linear matrix inequality method to alleviate the effects of the parameter uncertainties in the load and the working frequency of the WPT system. In the work of Xia et al. [20], a μ-controller designed by D-K iteration was used to reduce the influence of mutual inductance variation resulted from coil misalignment. Liang et al. [21] proposed an H_∞ control method with a selected weighting function considering parameter perturbations. Based on the Lyapunov–Krasovskii functional approach and the stochastic stability theory, Yu et al. [22] investigated the stability and control of a series–series WPT system considering capacitor uncertainties, time-varying delays and stochastic disturbances. The abovementioned researches demand an accurate mechanistic model of the WPT system before control design, which is difficult to obtain in applications with seawater medium. Considering the seawater environment, Yang et al. [23] proposed a nonlinear verified one-cycle control (NVOCC) method to regulate the output voltage of the undersea WPT system. For realizing both voltage and current control, Zheng et al. [24] proposed a proportional–integral (PI)-based double closed-loop control (PI-DCC) method. Besides, Li et al. [25] utilized a single variable inductor on the secondary side to achieve output current control of the undersea WPT systems and achieved system efficiency of 96.1%.

To overcome the difficulties of modeling the WPT system subjective to the seawater medium, the data-driven modeling could be a better option [26], [27], [28], [29], [30]. The data-driven modeling method infers a model for the system only from informative data of the input–output variables of the system, which is much easier to apply because data are quite easy to obtain in a open-loop system, in comparison to circuit topologies and component parameters that are typically expensive to precisely measure [26]. Chen et al. [26] proposed a refined instrumental variable (IV) method, which is based on the sampled data to model the WPT system with a phase-shift-controlled inverter. In their work, the data-driven modeling method is combined with the analytical modeling method to obtain better accuracy. Then, by considering the scenario of multitransmitter applications, Chen et al. [27] proposed an optimal refined IV method to model the multitransmitter WPT system with pure time delays based on the sampled input-output data. In the further step, Chen et al. [28] proposed a Hammerstein-model-based data-driven modeling method for the WPT system with a time-varying load, where the time-varying parameter is embedded into the the data-driven model to describe the time-varying characteristics of the system. For reducing the order of the mathematical model of the WPT system, they go on to develop a dynamic reduced-order data-driven modeling method to construct a low-order model of the WPT system without significant loss of accuracy, where the polynomial approximation technique is used for model order reduction [29]. Besides, Tang et al. [30] also proposed a sampled-data modeling method for WPT systems to make the model order equal to the system order. In addition to dynamic modeling applications, the artificial-intelligence-based methods are also developed to describe the nonlinear variable relationship using the input–output data for system optimizations. Choi and Kim [31] proposed a novel structure design of ferrite cores for WPT systems, where the deep neural network is trained to mapping the core distribution to the value of mutual inductance. Jeong et al. [32] proposed a Q-learning reinforcement learning (RL) algorithm to determine the optimal core distribution. Learning by trial-and-error, the RL algorithm will automatically find the optimal core structure.

Once the dynamic model is obtained, the model predictive control (MPC) algorithm is carried out to design the closed-loop control system. Extensive researches in dc–dc converters [33], [34], [35] have shown that the designed MPC will give superior performance if the model is correctly obtained and constraints have been properly specified. The MPC is also employed in WPT systems. Zhou et al. [36] proposed a MPC strategy for the receiving-side dc–dc converter to resist the power fluctuation for dynamic WPT process. Nevertheless, an extra dc–dc converter is introduced and the MPC controller demands extra sensors to form the state-feedback information for control action

calculations, which will increase the hardware cost and complexity. Without using dc–dc converter, MPC is used for the power control and maximum efficiency tracking of a bidirectional WPT system in [37]. The finite-control-set model predictive control (FCS-MPC) cooperates with pulse density modulation to ensure a fast dynamic response of the WPT system [38]. Then, Liu et al. [39] proposed a dynamic mathematical model-based FCS-MPC strategy for the active rectifier to achieve faster voltage regulation. However, it requires extra current sensors to sample the secondary coil current and the dc output current. To overcome this, in the work of Chen et al. [40], a FCS-MPC strategy with only one voltage sensor is proposed for the WPT systems, but an extra linear extended state observer is needed in the software level, which may increase the computation burden and decrease the dynamic response speed of the closed-loop WPT systems since the state observer takes time to estimate system-state values.

MPC can be regarded as an optimal control in a finite time domain. At each sampling time, the solution of the finite-horizon optimal control problem is obtained by the current state of the system. The solution is an optimal control sequence and the first control value in the sequence acts on the system [41]. By repeatedly performing optimization calculations on line and applying the optimal control value to the system, the MPC control system guarantees a fast regulating speed and robustness against disturbances [36].

The major contributions of this article can be summarized as follows.

1) To deal with the unknown dynamics of the WPT system in seawater environment for modeling, a data-driven modeling method using simplified refined instrumental variable (SRIV) algorithm is proposed to cover the dynamics from the seawater.
2) To improve dynamic response speed whilst dealing with the input constraints for safety considerations, the MPC algorithm with Hildreth's quadratic programming (QP) procedure is proposed.
3) This article achieves observer-free MPC control. The resulting MPC system is described using a special class of state-space models called nonminimal state-space (NMSS) models, which use plant input and output variables as its state variables. Hence, in the implementation of the predictive control system, an observer is not required.
4) For fair comparison with classical PI control, a specially-designed PI strategy is developed which uses the MPC dominant poles.

The rest of this article is organized as follows. The proposed WPT system is described in Section II and the control variable is analyzed. In Section III, the data-driven modeling process using the SRIV procedure and the method that converts it to a NMSS model are presented in details. The MPC control design is introduced in Section IV, followed by the experiment of the proposed MPC controller with comparison to the PI controller in Section V. A detailed power loss analysis of the closed-loop system is presented in Section VI. The comparison with the existing solutions for the control of the undersea WPT systems are presented in Section VII. Finally, Section VIII concludes this article.

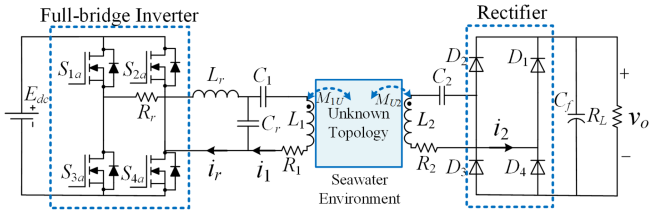

Fig. 2. Circuit topology of the proposed WPT System.

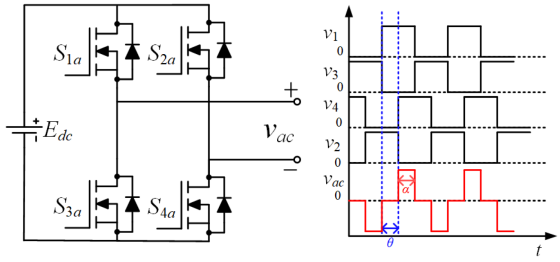

Fig. 3. Relevant voltage operating waveforms for phase-shift control.

II. System Description and Analysis of Control Variable

A. System Description of the WPT System

A LCC-S compensated WPT system consisting of three stages is considered in this article. Fig. 2 shows the circuit topology where L_1 denotes the inductance of the transmitter, L_2 denotes the inductance of the receiver, and L_r denotes the compensation inductor. C_1, C_2, and C_r denote the corresponding compensation capacitors, which obey the following constraints:

$$\omega L_r = \frac{1}{\omega C_r} = \omega L_1 - \frac{1}{\omega C_1}$$
$$\omega L_2 = \frac{1}{\omega C_2} \tag{1}$$

where $\omega = 2\pi f$ and f is the working frequency of the WPT system.

The input stage is a phase-shift-controlled full-bridge inverter that converts the dc voltage $E_{\rm dc}$ to a high-frequency square wave. The second stage is the WPT part. Considering there is a conductive water body between the transmitter and receiver, the energy will first interact with the water body through an unknown mutual inductance M_{1U} and then flow into the receiver through another unknown mutual inductance M_{U2}. The water body can be regarded as an unknown topology and the mechanism of how the energy crosses it is unknown. The last stage is a full-bridge rectifier with a low-pass filter, where in order to attenuate ripples of the output voltage v_o, a single capacitor C_f is used.

B. Analysis of the Control Variable

The output voltage of the inverter is controlled by the phase-shift pulse width modulation, and the voltage waveform is shown in Fig. 3. S_{1a}–S_{4a} are controlled switches, which are driven by square-wave signals v_1–v_4, respectively. $v_{\rm ac}$ is the output voltage of the inverter, θ is the shifting phase, and α is the conduction angle of the inverter.

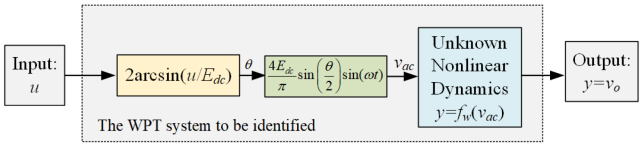

Fig. 4. Signal from control variable u to system output y.

Based on the formula of the Fourier trigonometric series, the output voltage v_{ac} can be expressed as

$$v_{\rm ac}(t) = \frac{4E_{\rm dc}}{\pi} \sum_{k=1,3,5,}^{+\infty} \frac{\sin\left(\frac{k\pi}{2}\right)\sin\left(\frac{k\theta}{2}\right)\sin\left(k\omega t\right)}{n}. \tag{2}$$

Owing to the filter characteristic of the compensation networks, the fundamental harmonic approximate method can be used to analyze the circuit [42]. The fundamental component of the output voltage of the inverter can be expressed as

$$v_{\rm ac}(t) \approx \frac{4E_{\rm dc}}{\pi}\sin\left(\frac{\theta}{2}\right)\sin(\omega t). \tag{3}$$

In practice, the dc supply $E_{\rm dc}$ is usually fixed and the shift-phase θ is the control variable. The output of the inverter can be described as $v_{\rm ac1} \approx (4E_{\rm dc}/\pi)\sin(\theta/2)\sin(\omega t)$. Then, we assume that the dc supply is a variable, which is represented by u and the shift-phase θ is fixed to π. In this situation, the output of the inverter can be described as $v_{\rm ac2} \approx (4u/\pi)\sin(\pi/2)\sin(\omega t)$. By letting $v_{\rm ac1} = v_{\rm ac2}$ to make the outputs of the inverter equal, it is obtained that

$$\frac{4E_{\rm dc}}{\pi}\sin\left(\frac{\theta}{2}\right)\sin(\omega t) = \frac{4u}{\pi}\sin\left(\frac{\pi}{2}\right)\sin(\omega t). \tag{4}$$

According to (4), the phase-shift angle of the inverter can be calculated as

$$\theta = 2\arcsin\left(\frac{u}{E_{\rm dc}}\right). \tag{5}$$

On the basis of the above relation, by selecting the control variable as u and then calculating the shifting phase θ, the amplitude of the input $v_{\rm ac}$ of the resonant tank can be controlled and the output voltage v_o of the WPT system can also be regulated. Fig. 4 shows the signal flow from the control variable u to the system output y, in which $y = f_w(v_{\rm ac})$ is a nonlinear mapping from $v_{\rm ac}$ to y. We should be aware that the unknown nonlinear mapping $y = f_w(v_{\rm ac})$ includes the unknown dynamics of the conductive medium and the switching nonlinearity of the rectifier. Our purpose is to construct a mapping from u to y using the input/output (I/O) data in the following section.

III. Data-Driven Modeling of the WPT System

A. Data-Driven Modeling of the WPT System Using the SRIV Method

The SRIV method uses a recursive least–square algorithm followed by the application of the IV method, which removes the bias of the estimates to obtain an accurate dynamic model [43].

Assume that the WPT system has structure of output error (OE) model

$$y(k) = \frac{B_u(z^{-1})}{A_u(z^{-1})}u(k) + n(k) \tag{6}$$

where

$$\begin{cases} A_u(z^{-1}) = 1 + a_1 z^{-1} + a_2 z^{-2} + \cdots + a_{n_a} z^{-n_a} \\ B_u(z^{-1}) = b_1 z^{-1} + b_2 z^{-2} + \cdots + b_{n_b} z^{-n_b} \end{cases} \tag{7}$$

in which z^{-1} is the unit-delay operator and k is the sampling instant. It should be noticed that $z^{-1}y(k) = y(k-1)$. A_u and B_u are the polynomials of z^{-1}. $\{a_1, a_2, \ldots a_{n_a}\}$ and $\{b_1, b_2, \ldots b_{n_b}\}$ are the coefficients of A_u and B_u, respectively. n_a denotes the order of the denominator polynomial while n_b denotes the order of the numerator polynomial. $n(k)$ is the measurement noise with zero mean value. Then, (6) can be written as

$$\begin{aligned} & y(k)A_u\left(z^{-1}\right) = B_u(z^{-1})u(k) + n(k)A_u(z^{-1}) \\ & \Rightarrow y(k)\left(1 + a_1 z^{-1} + a_2 z^{-2} + \cdots + a_{n_a} z^{-n_a}\right) \\ & = u(k)\left(b_1 z^{-1} + b_2 z^{-2} + \cdots + b_{n_b} z^{-n_b}\right) + A_u(z^{-1})n(k) \\ & \Rightarrow y(k) + \sum_{i=1}^{n_a} a_i y(k-i) = \sum_{j=1}^{n_b} b_j u(k-j) + A_u(z^{-1})n(k). \end{aligned} \tag{8}$$

From (8), we have

$$y(k) = -\sum_{i=1}^{n_a} a_i y(k-i) + \sum_{j=1}^{n_b} b_j u(k-j) + A_u(z^{-1})n(k). \tag{9}$$

By defining

$$\begin{cases} \varepsilon(k) \triangleq A_u(z^{-1})n(k) \\ \phi(k) \triangleq [-y(k-1), \ldots, -y(k-n_a) \\ u(k), \ldots, u(k-n_b)]^T \\ \vartheta \triangleq [a_1, \ldots, a_{n_a}, b_1, \ldots, b_{n_b}]^T. \end{cases} \tag{10}$$

Equation (9) can be rewritten as a compact vector-form

$$y(k) = \phi^T(k)\vartheta + \varepsilon(k). \tag{11}$$

Assume that we already obtain L pairs of I/O data $\{(u(i), y(i))\}, i = 1, 2, \ldots, L$. Filling these data into $y(k)$ and $\phi(k)$, we have

$$\begin{cases} y(1) = \phi^T(1)\vartheta + \varepsilon(1) \\ y(2) = \phi^T(2)\vartheta + \varepsilon(2) \\ \cdots \\ y(L) = \phi^T(L)\vartheta + \varepsilon(L). \end{cases} \tag{12}$$

It should be declared that $y(k) = 0, k \le 0$ and $\varepsilon(i), i = 1, \ldots, L$ are unknown data, which are related to the sampling noise. From (12), the observation equation can be written as

$$Y_L = \Phi_L\vartheta + \mathrm{E}_L \tag{13}$$

where (14), shown at the bottom of the next page. The purpose of the data-driven modeling is to estimate the vector of parameters ϑ using the historical data Y_L and Φ_L.

Construct a cost function of ϑ, which represent the error between the output of the OE model and the measurement data of y

$$\begin{aligned} J(\vartheta) &= (Y_L - \Phi_L\vartheta)^T(Y_L - \Phi_L\vartheta) \\ &= Y_L^T Y_L - 2\vartheta^T\Phi_L^T Y_L + \vartheta^T\Phi_L^T\Phi_L\vartheta. \end{aligned} \tag{15}$$

Letting

$$\frac{\partial J(\vartheta)}{\partial \vartheta} = 0 \tag{16}$$

to minimize the cost function, the least–squares estimation of ϑ is

$$\hat{\vartheta}_{LS} = (\Phi_L^T \Phi_L)^{-1} \Phi_L^T Y_L = [\hat{a}_1, \ldots, \hat{a}_{n_a}, \hat{b}_1, \ldots, \hat{b}_{n_b}]^T. \tag{17}$$

It can be observed that A_u and B_u are the functions of the vector ϑ. As the estimation $\hat{\vartheta}_{LS}$ is obtained, A_u and B_u can be reconstructed as the functions of $\hat{\vartheta}_{LS}$

$$\begin{cases} A_u(z^{-1}, \hat{\vartheta}_{LS}) = 1 + \hat{a}_1 z^{-1} + \hat{a}_2 z^{-2} + \cdots + \hat{a}_{n_a} z^{-n_a} \\ B_u(z^{-1}, \hat{\vartheta}_{LS}) = \hat{b}_1 z^{-1} + \hat{b}_2 z^{-2} + \cdots + \hat{b}_{n_b} z^{-n_b}. \end{cases} \tag{18}$$

Introduce a new variable, which is called IV

$$\widehat{h}(k) = \frac{B_u(z^{-1}, \hat{\vartheta}_{LS})}{A_u(z^{-1}, \hat{\vartheta}_{LS})} u(k). \tag{19}$$

Along the same light of the derivation of (8), it can be derived that

$$\hat{h}(k) = -\sum_{i=1}^{n_a} a_i \hat{h}(k-i) + \sum_{j=1}^{n_b} b_j u(k-j). \tag{20}$$

Assume that $\hat{h}(k) = 0, k \leq 0$. With the estimation value $\{\hat{a}_1, \ldots, \hat{a}_{n_a}, \hat{b}_1, \ldots, \hat{b}_{n_b}\}$ and the input data $u(i), i = 1, 2, \ldots, L$, we can calculate $\hat{h}(k-i), i = 1, 2, \ldots, n_a$ iteratively via (20).

By defining

$$\hat{\phi}^T(k) \triangleq [-\hat{h}(k-1), \ldots, -\hat{h}(k-n_a), u(k), \ldots, u(k-n_b)]^T. \tag{21}$$

Equation (20) can be rewritten as a vector-form

$$\hat{h}(k) = \hat{\phi}^T(k) \hat{\vartheta}_{LS}. \tag{22}$$

Then, we construct an instrumental information matrix (23), shown at the bottom of this page. Construct a new cost function of ϑ based on the instrumental information matrix $\hat{\Phi}_L$

$$J_{\text{IV}}(\vartheta) = (Y_L - \hat{\Phi}_L \vartheta)^T (Y_L - \hat{\Phi}_L \vartheta). \tag{24}$$

Algorithm 1: SRIV.

Input:
- Sampled data: $\{y(k), u(k)\}_{k=1}^{L}$;
- Polynomial degrees: $\{n_a, n_b\}$;
- Number of iterations: N_{iter};
- Tolerances: ς_{tol}.

Output: $\vartheta^* \triangleq [a_1^*, \ldots, a_{n_a}^*, b_1^*, \ldots, b_{n_b}^*]^T$;

based on the sampled data $\{y(k), u(k)\}_{k=1}^{L}$, construct $\{Y_L, \Phi_L\}$ and estimate ϑ^0 via the least squares method using (17);
for $j \leftarrow 1$ **to** N_{iter} **do**
  for $i \leftarrow 1$ **to** L **do**
    compute $\hat{\phi}^T(i)$ using $\widehat{h}(i) = \hat{\phi}^T(i) \hat{\vartheta}^{j-1}$;
  end
  construct $\hat{\Phi}_L$;
  compute $\vartheta^j = (\hat{\Phi}_L^T \Phi_L)^{-1} \hat{\Phi}_L^T Y_L$
  if $\|\vartheta^j - \vartheta^{j-1}\|_\infty < \varsigma_{\text{tol}}$ **then** break
end
$\vartheta^* \leftarrow \vartheta^j$;

Minimizing the $J_{\text{IV}}(\vartheta)$ with respect to ϑ, the IV estimation of ϑ can be obtained as

$$\hat{\vartheta}_{IV} = \left(\hat{\Phi}_L^T \Phi_L\right)^{-1} \hat{\Phi}_L^T Y_L. \tag{25}$$

Let $\hat{\vartheta}_{\text{LS}} = \hat{\vartheta}_{\text{IV}}$ and start a new cycle from (19) to (25), the estimation of ϑ will be updated again. Repeat the updating procedure until the estimation converges, and the final estimation of ϑ can be obtained, which is represented as $\vartheta^* = [a_1^*, \ldots, a_{n_a}^*, b_1^*, \ldots, b_{n_b}^*]^T$. The complete SRIV algorithm can be summarized in Algorithm 1, where $\|\cdot\|_\infty$ denotes the maximum element of a vector.

After the SRIV procedure, the data-driven model of the WPT system can be obtained as

$$y(k) = \frac{B_u(z^{-1}, \vartheta^*)}{A_u(z^{-1}, \vartheta^*)} u(k). \tag{26}$$

$$\begin{aligned} Y_L &= [y(1), y(2), \ldots, y(L)]^T \\ \mathrm{E}_L &= [\varepsilon(1), \varepsilon(2), \ldots, \varepsilon(L)]^T \\ \Phi_L &= [\phi^T(1), \phi^T(2), \ldots, \phi^T(L)]^T \\ &= \begin{bmatrix} -y(0) & \cdots & -y(1-n_a) & u(0) & \cdots & u(1-n_b) \\ -y(1) & \cdots & -y(2-n_a) & u(1) & \cdots & u(2-n_b) \\ \vdots & \vdots & \vdots & \vdots & \vdots & \vdots \\ -y(L-1) & \cdots & -y(L-n_a) & u(L-1) & \cdots & u(L-n_b) \end{bmatrix}_{L \times (n_a + n_b)}. \end{aligned} \tag{14}$$

$$\begin{aligned} \hat{\Phi}_L &= [\hat{\phi}^T(1), \hat{\phi}^T(2), \ldots, \hat{\phi}^T(L)]^T \\ &= \begin{bmatrix} -\hat{h}(0) & \cdots & -\hat{h}(1-n_a) & u(0) & \cdots & u(1-n_b) \\ -\hat{h}(1) & \cdots & -\hat{h}(2-n_a) & u(1) & \cdots & u(2-n_b) \\ \vdots & \vdots & \vdots & \vdots & \vdots & \vdots \\ -\hat{h}(L-1) & \cdots & -\hat{h}(L-n_a) & u(L-1) & \cdots & u(L-n_b) \end{bmatrix}_{L \times (n_a + n_b)}. \end{aligned} \tag{23}$$

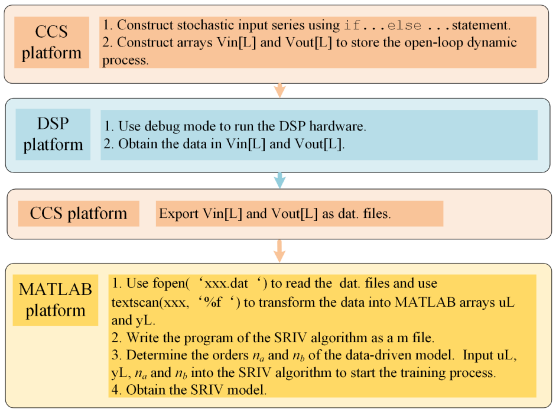

Fig. 5. Training process of the SRIV data-driven model.

In practice, the training process of the data-driven model takes advantages of three different platforms, including Code Composer Studio (CCS), digital signal processing (DSP) hardware, and MATLAB. The DSP hardware is used to generate control inputs for the WPT system. The CCS is used to flash the program for the DSP control board and record the process data. At last, MATLAB will train the model based on the exported data from the CCS. The training process regarding the data collection process is summarized in Fig. 5. The data-driven modeling of the WPT system is an offline training process. The paired I/O data of the system should be collected by implementing an open-loop test, and then store them into two different data vectors Vin[L] and Vout[L], where L is the length of the vectors. In practice, L can be set between 800 and 2000. The training process can be completed in only a few iterations.

Remark 1: By the inherent optimal IV nature of the SRIV algorithm, the I/O data subject to the colored noise can be filtered [43], thus generating a more accurate model with no bias.

Remark 2: The identified model is a small-signal model since the data sets are obtained around a static operating point and it only considers one operating condition.

B. NMSS Realization of the WPT System

MPC utilizes state feedback information to calculate control values. As the high-frequency oscillating state variables are hard to measure online for WPT systems, the observer should be adopted to estimate the state variables. However, the presence of the observer is also a problem in more general terms since it can lead to robustness problems and "loop transfer recovery" demands [44]. To avoid introducing an observer in MPC design, the special NMSS model structure is used to construct the dynamic model of the WPT system [45].

Based on the data-driven model (26), the discrete-time transfer function of the WPT system can be written as

$$\frac{y(k)}{u(k)}=\frac{b_1^*+b_2^*z^{-1}+\cdots+b_{n_b}^*z^{-n_b+1}}{z+a_1^*+a_2^*z^{-1}+\cdots+a_{n_a}^*z^{-n_a+1}}. \tag{27}$$

Using (27), the output of the WPT system at instant $k+1$ can be obtained as

$$y(k+1)=-\sum_{i=1}^{n_a}a_i^*y(k-i+1)+\sum_{j=1}^{n_b}b_j^*u(k-j+1). \tag{28}$$

Construct a state vector $x_m(k)$ by selecting the following state variables from (28)

$$x_m(k)=[y(k),y(k-1),\ldots,y(k-n_a+1)\quad u(k-1),\ldots,u(k-n_b+1)]^T. \tag{29}$$

Let $x_m(k)$ shift one step forward to obtain

$$x_m(k+1)=[y(k+1),y(k),\ldots,y(k-n_a+2)\quad u(k),\ldots,u(k-n_b+2)]^T. \tag{30}$$

Investigating the relationship between $x_m(k+1)$ and $x_m(k)$ based on (28) and letting the $u(k)$ be the control input, a special state space constructed by the I/O data, which is called NMSS can be easily obtained as written in (31), shown at the bottom of the next page.

Let A_m denote the $(n_a+n_b-1)\times(n_a+n_b-1)$ square matrix in (31) and $B_m=[b_1^*,0,\ldots,0,0,1,0,\ldots,0,0]^T_{(na+nb-1)1}$, the NMSS model can be represented as

$$x_m(k+1)=A_mx_m(k)+B_mu(k). \tag{32}$$

It should be noted that there are one $(n_a-1)\times(n_a-1)$ identity matrix and one $(n_b-2)\times(n_b-2)$ identity matrix in the top left corner and bottom right corner of A_m, respectively.

Remark 3: A state-space realization of a system is a NMSS means that the state-space model is controllable but unobservable by checking the rank of the controllability matrix and observability matrix.

IV. MPC Design

A. Augmented State-Space Model of the WPT System

Taking a difference operation on both sides of (31) to embed the integral action [45], we obtain

$$\Delta x_m(k+1)=A_m\Delta x_m(k)+B_m\Delta u(k) \tag{33}$$

where

$$\begin{cases}\Delta x_m(k+1)=x_m(k+1)-x_m(k)\\ \Delta x_m(k)=x_m(k)-x_m(k-1)\\ \Delta u(k)=u(k)-u(k-1).\end{cases} \tag{34}$$

Then, we define a new state variable vector to connect $\Delta x_m(k)$ to the output $y(k)$

$$x(k)=\begin{bmatrix}\Delta x_m(k)^T & y(k)\end{bmatrix}^T. \tag{35}$$

Assuming that the dimension of x_m is n_1, this new state variable vector leads to the following state-space model

$$\begin{cases}x(k+1)=Ax(k)+B\Delta u(k)\\ y(k)=Cx(k)\end{cases} \tag{36}$$

where

$$\begin{cases}A=\begin{bmatrix}A_m & o_m^T\\ C_mA_m & 1\end{bmatrix},B=\begin{bmatrix}B_m\\ C_mB_m\end{bmatrix}\\ C=\begin{bmatrix}o_m & 1\end{bmatrix},o_m=\overbrace{\begin{bmatrix}0 & 0 & \cdots & 0\end{bmatrix}}^{n_1}.\end{cases} \tag{37}$$

The triplet (A, B, C) is called the augmented model which will be used in the design of predictive control.

B. MPC With Operational Constraints

The MPC utilizes the receding horizon optimization technique to calculate the control actions. Before we represent the MPC procedure, some concepts should be defined first. Assuming that the sampling instant is $k_i, k_i > 0$. The control horizon is N_c, which denotes the number of parameters used to capture the future control trajectory. The prediction horizon is N_p which denotes the number of the N_p-step future predictions of the WPT system, and N_p is also the length of the optimization window.

Based on the augmented model (A, B, C), we can derive the prediction equation state variables as follows:

$$x(k_i + N_p\,|k_i\,) = A^{N_p}x(k_i) + \sum_{j=0}^{N_c-1} A^{N_p-j-1}B\Delta u(k_i + j). \tag{38}$$

From the predicted state variables, the predicted output variable is

$$y(k_i+N_p\,|k_i\,)=CA^{N_p}x(k_i)+\sum_{j=0}^{N_c-1} CA^{N_p-j-1}B\Delta u(k_i+j). \tag{39}$$

Defining vectors

$$\begin{cases} Y \triangleq [y(k_i + 1\,|k_i\,), y(k_i + 2\,|k_i\,), \ldots, y(k_i + N_p\,|k_i\,)]^T \\ \Delta U = [\Delta u(k_i), \Delta u(k_i + 1), \ldots, \Delta u(k_i + N_c - 1)]^T \end{cases} \tag{40}$$

and combining (39) with (40), we can obtain the following prediction equation:

$$Y = Fx(k_i) + \Theta\Delta U \tag{41}$$

where

$$F = [CA, CA^2, CA^3, \ldots, CA^{N_p}]^T \tag{42}$$

$$\Theta = \begin{bmatrix} CB & 0 & 0 & \ldots & 0 \\ CAB & CB & 0 & \ldots & 0 \\ CA^2B & CAB & CB & \ldots & 0 \\ \vdots & & & & \\ CA^{N_p-1}B & CA^{N_p-2}B & CA^{N_p-3}B & \ldots & CA^{N_p-N_c}B \end{bmatrix}. \tag{43}$$

Assume that the data vector that contains the reference voltage V_{ref} is

$$R_V^T = \begin{bmatrix} 1 & 1 & \ldots & 1 \end{bmatrix}_{1\times N_p} V_{\text{ref}}. \tag{44}$$

We define the cost function J_m that reflects the control objective as

$$J_m = (R_V - Y)^T(R_V - Y) + \Delta U^T R_u \Delta U \tag{45}$$

where

$$R_u = r_w I_{N_c\times N_c}. \tag{46}$$

The first term of (45) is linked to the objective of minimizing the errors between the output and the reference voltage while the second term reflects the consideration to limit the variation of ΔU. $r_w \geq 0$ is a tuning parameter to increase the flexibility of the algorithm.

By substituting (41) into (45), the cost function can be rewritten as

$$\begin{aligned} J_m = {} & (R_V - Fx(k_i))^T(R_V - Fx(k_i)) \\ & - 2\Delta U^T\Theta^T(R_V - Fx(k_i)) \\ & + \Delta U^T\left(\Theta^T\Theta + R_u\right)\Delta U. \end{aligned} \tag{47}$$

Taking the first derivative of the cost function J_m with respect to ΔU, and letting $\partial J_m/\partial\Delta U = 0$, the optimal solution for the control action without hard constraints is

$$\Delta U = \left(\Theta^T\Theta + R_u\right)^{-1}\Theta^T(R_V - Fx(k_i)). \tag{48}$$

Consider the constraints on the amplitude of the control input $u(k_i)$

$$\begin{aligned} & u^{\min} \leq u(k_i) \leq u^{\max} \\ & u^{\min} \leq u(k_i + 1) \leq u^{\max} \\ & \qquad \ldots \\ & u^{\min} \leq u(k_i + N_c - 1) \leq u^{\max} \end{aligned}$$

$$\begin{bmatrix} y(k+1) \\ y(k) \\ \vdots \\ y(k-n_a+3) \\ y(k-n_a+2) \\ u(k) \\ u(k-1) \\ \vdots \\ u(k-n_b+3) \\ u(k-n_b+2) \end{bmatrix} = \left[\begin{array}{cccccccccc} -a_1^* & -a_2^* & \ldots & -a_{n_a-1}^* & -a_{n_a}^* & b_2^* & b_3^* & \ldots & b_{n_b-1}^* & b_{n_b}^* \\ 1 & 0 & \ldots & 0 & 0 & 0 & 0 & \ldots & 0 & 0 \\ 0 & 1 & \ldots & 0 & 0 & 0 & 0 & \ldots & 0 & 0 \\ \vdots & \vdots & \ddots & \vdots & \vdots & \vdots & \vdots & \ldots & \vdots & \vdots \\ 0 & 0 & \ldots & 1 & 0 & 0 & 0 & \ldots & 0 & 0 \\ \hline 0 & 0 & \ldots & 0 & 0 & 0 & 0 & \ldots & 0 & 0 \\ 0 & 0 & \ldots & 0 & 0 & 1 & 0 & \ldots & 0 & 0 \\ \vdots & \vdots & \ldots & \vdots & \vdots & \vdots & \ddots & \ldots & \vdots & \vdots \\ 0 & 0 & \ldots & 0 & 0 & 0 & \ldots & 1 & \ldots & 0 \\ 0 & 0 & \ldots & 0 & 0 & 0 & 0 & \ldots & 1 & 0 \end{array}\right] \begin{bmatrix} y(k) \\ y(k-1) \\ \vdots \\ y(k-n_a+2) \\ y(k-n_a+1) \\ u(k-1) \\ u(k-2) \\ \vdots \\ u(k-n_b+2) \\ u(k-n_b+1) \end{bmatrix} + \begin{bmatrix} b_1^* \\ 0 \\ \vdots \\ 0 \\ 0 \\ 1 \\ 0 \\ \vdots \\ 0 \\ 0 \end{bmatrix} u(k). \tag{31}$$

where $u^{\min}$ and $u^{\max}$ denote, respectively, the allowed minimum value and maximum value of the control input $u(k_i)$ during the control process.

Define vectors

$$U \triangleq [u(k_i), u(k_i+1), \ldots, u(k_i+N_c-1)]^T \tag{49}$$

$$D_1 \triangleq \begin{bmatrix} 1 & 1 & \ldots & 1 \end{bmatrix}^T_{1\times N_c} \tag{50}$$

and a lower triangular matrix

$$D_2 \triangleq \begin{bmatrix} 1 & 0 & \cdots & 0 \\ 1 & 1 & \cdots & 0 \\ \vdots & & \ddots & \\ 1 & 1 & \ldots & 1 \end{bmatrix}_{N_c\times N_c}. \tag{51}$$

The control vector U can be represented as the affine function of ΔU

$$U = D_1 u(k_i-1) + D_2 \Delta U. \tag{52}$$

Then, the constraints for the control actions can be imposed as

$$\begin{aligned} -(D_1 u(k_i-1) + D_2\Delta U) &\le -U^{\min} \\ D_1 u(k_i-1) + D_2\Delta U &\le U^{\max} \end{aligned} \tag{53}$$

where

$$\begin{cases} U^{\min} = \begin{bmatrix} 1 & 1 & \ldots & 1 \end{bmatrix}^T_{1\times N_c} u^{\min} \\ U^{\max} = \begin{bmatrix} 1 & 1 & \ldots & 1 \end{bmatrix}^T_{1\times N_c} u^{\max}. \end{cases} \tag{54}$$

Finally, the MPC in the presence of hard constraints on the control input $u(k_i)$ is proposed as finding the parameter vector ΔU that minimizes J_m subject to the inequality constraints

$$M_u \Delta U \le N_u \tag{55}$$

where the data matrices are

$$M_u = \begin{bmatrix} -D_2 \\ D_2 \end{bmatrix}, N_u = \begin{bmatrix} -U^{\min} + D_1 u(k_i-1) \\ U^{\max} - D_1 u(k_i-1) \end{bmatrix}. \tag{56}$$

Hence, the computation of the control action is transformed into a QP problem.

It should be noted that the first term of J_m is not related to ΔU, and hence the real part for optimization in J_m can be represented as

$$J_r = \frac{1}{2}\Delta U^T E_r \Delta U + \Delta U^T F_r \tag{57}$$

where

$$E_r = \left(2\Theta^T\Theta + 2R_u\right), F_r = -2\Theta^T(R_V - Fx(k_i)). \tag{58}$$

At the time instant k_i, we assume that the data of $u(k_i-1)$ is obtained. Hence, N_u is known at k_i. In order to obtain the constrained optimal solution, a matrix M_{act} is constructed with only the active inequality constraints in (55) (which means that the inequalities are violated). By using the Hildreth's QP procedure [46] to find the Lagrange multipliers λ_{act} [45], the resulting constrained optimal solution can be derived as

$$\Delta U^* = -E_r^{-1}(F_r + M_{\text{act}}^T \lambda_{\text{act}}). \tag{59}$$

Because of the receding horizon control principle, we only take the first element of ΔU^* at time k_i as the incremental control, thus

$$\begin{aligned} \Delta u(k_i) &= \begin{bmatrix} 1 & 0 & \ldots & 0 \end{bmatrix}_{1\times N_c} \Delta U^* \\ &= -\begin{bmatrix} 1 & 0 & \ldots & 0 \end{bmatrix}_{1\times N_c} E_r^{-1}(F_r + M_{\text{act}}^T \lambda_{\text{act}}). \end{aligned} \tag{60}$$

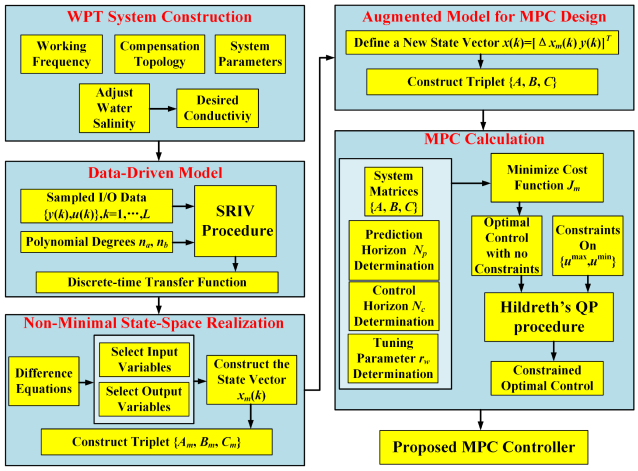

Fig. 6. Design flow chart of the MPC method.

TABLE I
PARAMETER VALUES OF THE PROPOSED WPT SYSTEM

Parameters	Values
Switching frequency f (kHz)	40
Conductivity c (mS/cm)	49.0
Power transfer distance d_0 (cm)	20
Filter capacitance C_f (μF)	220
Load R_L (Ω)	10
Input DC voltage E_{dc} (V)	30
Primary capacitance C_1 (nF)	141.5
Primary capacitance C_r (μF)	1.58
Inductance of the transmitting coil L_1 (μH)	124
Compensation inductance L_r (μH)	10.5
Secondary capacitance C_2 (nF)	120
Inductance of the pick-up coil L_2 (μH)	122

TABLE II
PARAMETER VALUES OF THE COUPLING STRUCTURE

Parameters	Values
Number of turns N_1	16
Length l_1 (cm)	30
Width w_1 (cm)	30
Diameter of wires d_1 (mm)	5
Depth of the cores h_1 (mm)	5

The design process of the MPC method for WPT systems is summarized as a flow chart shown in Fig. 6. It should be noted that the proposed MPC design is based on the identified small signal model. When large disturbances occur to threaten the system stability, a new system model should be identified and the MPC parameters should also be updated.

V. EXPERIMENTAL VALIDATIONS

An experimental prototype is established to verify the superiority of the MPC controller. The system parameters are shown in Table I and the configuration of the closed-loop system is shown in Figs. 7 and 9 is its corresponding equivalent circuit. The structure of the coupling coils is presented in Fig. 8 and the corresponding parameter values are shown in Table II. A 150 cm × 150 cm × 70 cm glass water tank with conductive water is used to simulate the seawater environment. A

Fig. 7. Experimental platform.

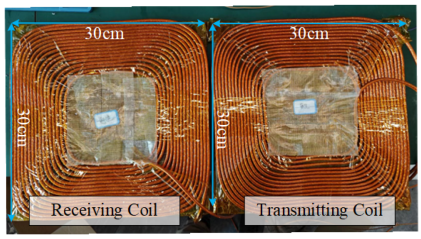

Fig. 8. Structure of the coupling coils.

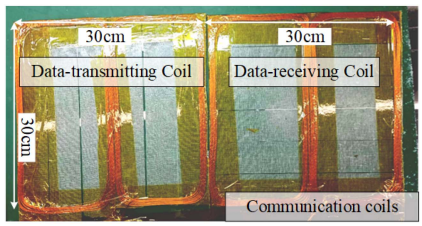

Fig. 10. Structure of the communication coils.

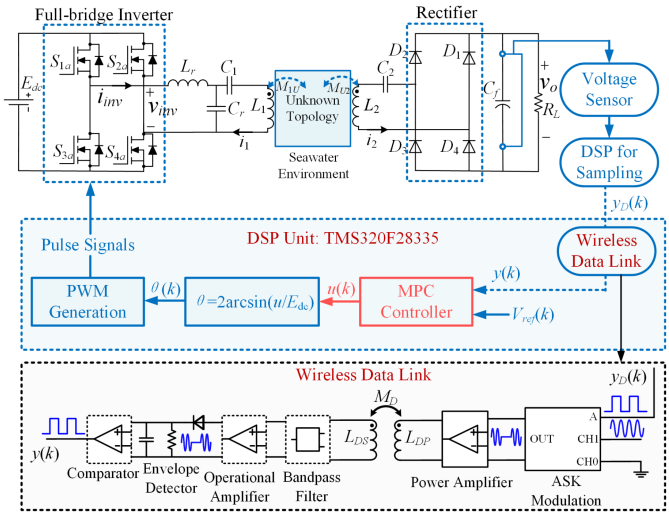

Fig. 9. Equivalent circuit of the experimental prototype.

quadrupole conductivity meter is used to detect the conductivity of the water. The ITECH programmable dc power supply is used to power the WPT system and the NGI bidirectional power supply is used to simulate the load.

A. Simultaneous Wireless Power and Data Transfer (SWPDT)

In order to overcome the large damping of classical communication method (such as Wifi and Blue tooth) in seawater [47], a data-parallel transmission method (SWPDT) is utilized to meet control signal information transmission between primary and secondary side [48]. A pair of bipolar coils with the same size are used to transfer the voltage information from the secondary side back to the primary side, which is shown in Fig. 10. The turns of both coils are 6, the inductance L_{DP} of the data-transmitting coil is 60.1 μH, and the inductance L_{DS} of the data-receiving coil is 60.3 μH. The mutual inductance M_D between the communication coils (in air) is about 2 μH. The communication coils are winded on the acrylic boards to form the communication cards.

As can be seen from Fig. 9, the processing circuit to implement the data transfer consists of an amplitude shift keying (ASK) modulation module achieved by BL1551 chip, a power amplifier achieved by RS8752 chip, a bandpass filter by using ceramic filter, an envelope detector, an operational amplifier achieved by RS8752 chip, and a comparator also by using RS8752 chip. The operating frequency of the data transfer channel is 10 MHz. The data transfer rate is 19.2 kbps. There are two controllers, i.e., primary DSP controller and secondary DSP controller. Secondary DSP controller samples the output voltage v_o by using ADC module after the sampling circuit, and then transforms the data into binary form $y_D(k)$. The binary data will be transferred into the general-purpose input/output (GPIO) pin of DSP in the form of high and low levels and then be injected into the data transfer channel.

B. Data-Driven Modeling of the WPT Prototype

To build the model of the system, where the data for model identification were acquired from an open-loop system, the data-driven modeling method is first implemented. The sampling interval is 1 ms. To obtain better identification results, the data should be informative as much as possible. This is typically done by selecting an excitation sequence that is rich in harmonics, such as pseudorandom sequences. Moreover, it is expected that the output response contains both static parts and transient parts.

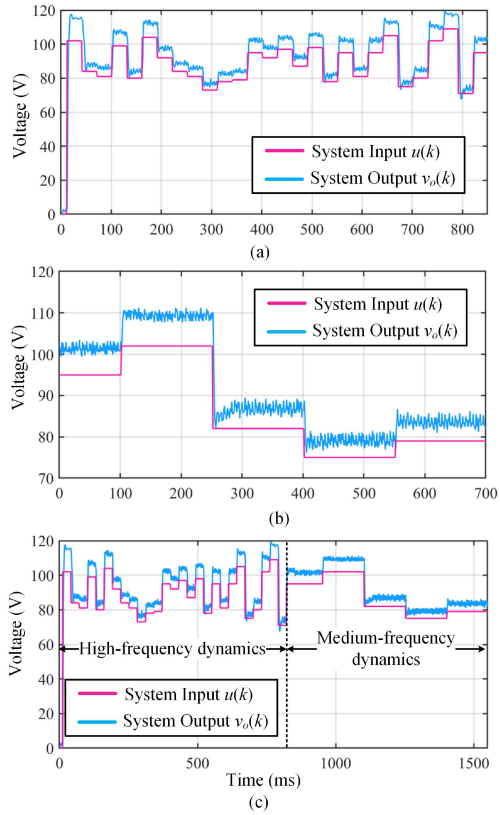

Fig. 11. Dynamics of the WPT system. (a) High-frequency dynamics. (b) Medium-frequency dynamics. (c) Combination of two different dynamic response.

Hence, the system input sequences is consisted of two parts. The first part is the high-frequency part that is used to generate enough transient information in the output. The second part is the medium-frequency part, which varies at a slower speed to make the output includes static information. The DSP unit TMS320F28335 is used for sending preset control action $u(k)$, which will be translated to the shifting phase $\theta(k)$ later to the full-bridge inverter. Assuming that the settling time of the open-loop WPT system is T_s, the switching time of the system input sequences $u(k)$ should be set to less than T_s. In this article, the system input sequences of the high-frequency part is given as

$$\begin{aligned} u(k) = 102 &\overset{T_1}{\to} 84 \overset{T_1}{\to} 81 \overset{T_1}{\to} 99 \overset{T_1}{\to} 80 \\ &\overset{T_1}{\to} 104 \overset{T_1}{\to} 92 \overset{T_1}{\to} 84 \overset{T_1}{\to} 81 \overset{T_1}{\to} 73 \overset{T_1}{\to} 78 \\ &\overset{T_1}{\to} 79 \overset{T_1}{\to} 95 \overset{T_1}{\to} 92 \overset{T_1}{\to} 97 \overset{T_1}{\to} 87 \overset{T_1}{\to} 98 \\ &\overset{T_1}{\to} 78 \overset{T_1}{\to} 95 \overset{T_1}{\to} 81 \overset{T_1}{\to} 95 \overset{T_1}{\to} 105 \overset{T_1}{\to} 75 \\ &\overset{T_1}{\to} 80 \overset{T_1}{\to} 102 \overset{T_1}{\to} 109 \overset{T_1}{\to} 71 \overset{T_1}{\to} 95(V) \end{aligned} \tag{61}$$

where the switching time T_1 is 30 ms and $102 \to^{T_1} 84$ means the reference voltage switches from 102 to 84 V after a duration of T_1. The response $v_o(k)$ of the system input sequences $u(k)$ is shown in Fig. 11(a), from which it is clear that, due to T_1 which is too short (30 ms), the system has not reached a steady state in each duration time of $u(k)$, so the sampled output data contains an insufficient amount of static information about system. If system identification is conducted based on this dataset, the static gain of the system may not be correctly captured. To avoid this problem, we should enlarge the duration time so that the static information of the system can be stimulated.

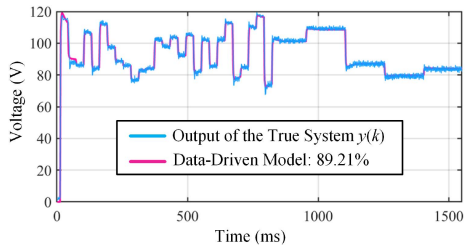

Fig. 12. Comparison of the measured output and estimated model output.

The second part of the system input sequences is the medium-frequency part, which is given as

$$u(k) = 95 \overset{T_2}{\to} 102 \overset{T_2}{\to} 82 \overset{T_2}{\to} 75 \overset{T_2}{\to} 79(V) \tag{62}$$

where the switching time T_2 is 150 ms. The response $v_o(k)$ is shown in Fig. 11(b). The next step is to combine the I/O data of the high-frequency part with the medium-frequency part, which is shown in Fig. 11(c). To quantify the explanatory ability of the estimated model, the fit ratio defined below is used as the performance index

$$\text{fitness} = \left(1 - \frac{\|Y - Y_s\|_2}{\|Y - \text{mean}\{Y\}\|_2}\right) \cdot 100\% \tag{63}$$

where Y and Y_s stand for sampled output and the simulated output by using the estimated model, respectively. By using Algorithm 1, a fifth-order discrete-time transfer function model with 89.21% fitness is generated as follows:

$$\begin{cases} G_h(z) = \frac{B_h(z^{-1})}{A_h(z^{-1})} \\ B_h(z^{-1}) = 0.3556z^{-1} + 0.2926z^{-2} - 0.4133z^{-3} \\ \quad -0.1892z^{-4} \\ A_h(z^{-1}) = 1 - 1.013z^{-1} + 0.08977z^{-2} - 0.02487z^{-3} \\ -0.03273z^{-4} + 0.02121z^{-5}. \end{cases} \tag{64}$$

Fig. 12 depicts the comparison between the output of the data-driven model with the output of the true system. It can be seen that the data-driven model coincides very well with the true system output, except for the short time interval around $t = 20$ ms, in which a marginally larger deviation can be observed.

Remark 4: Assume that the transient time of the open-loop WPT system is T_s. A stochastic excitation series with duration $T_1 = 0.3 \sim 0.5T_s$ is defined as a high-frequency excitation series. A stochastic excitation series with duration $T_2 = 0.6 \sim 1.2T_s$ is defined as a medium-frequency excitation series.

C. MPC Implementation

The state-feedback control form of (48) can be written as

$$\Delta u(k) = K_y V_{\text{ref}}(k) - K_{\text{mpc}} x(k). \tag{65}$$

From the structure of (65), it can be seen that the proposed MPC control is a two-degree-of-freedom (DoF) control since the control action utilizes the information of the state $x(k)$ and the reference $V_{\text{ref}}(k)$, rather than the mixed information, i.e, the difference $e(k) = V_{\text{ref}}(k) - y(k)$.

Based on (64), the parameters of the NMSS realization $\{A_m, B_m, C_m\}$ of the data-driven model are $a_1^* = -0.8717, a_2^* = -0.195, a_3^* = 0.06733, a_4^* = 0.005817, a_5^* = 0.03124, b_1^* = 0.348, b_2^* = 0.1738, b_3^* = -0.2621,$ and $b_4^* = -0.2197$. Based on the estimated parameters, the augmented model $\{A, B, C\}$ can be easily obtained according to (37). The prediction horizon N_p is chosen as 100, the control horizon N_c is chosen as 10 and the tuning parameter r_w is set as 14, and then the control action $u(k)$ can be computed via (65), where

$$\begin{cases} K_{mpc} = [1.3234, 0.1556, 0.1556, -0.0444, -0.0426 \\ \qquad -0.2851, -0.6142, -0.2998, 0.2361]^T \\ K_y = 0.2361. \end{cases} \tag{66}$$

The control process can be described as follows: the output voltage v_o is measured and quantized via the ADC block of the DSP controller on the secondary side, and then transmitted to the primary-side controller via the data-transfer channel. Once the primary-side DSP has received this output data, it computes an optimal $\theta(k)$ using the output feedback data and the reference signal via the MPC algorithm. Finally, the embedded enhanced pulsewidth modulation module is updated using the latest $\theta(k)$ to generate the driving signals $v_1 - v_4$ of the full-bridge inverter. The abovementioned procedure will be repeated in each control period.

The effect of the MPC controller is verified via four experiments: the reference tracking with input amplitude constraints, the load perturbations, the water flow disturbance, and the horizontal misalignment tolerance. The communication waveforms are affiliated to every experimental test, including the DSP GPIO output, the ASK modulation output in the secondary side, the operational amplifier output and the demodulated data in the primary side. The utilized oscilloscope for recording the communication experimental waveforms is Tektronix TPS2024B and the oscilloscope for recording the power experimental waveforms is Tektronix 3 series mixed domain oscilloscope.

1) Dynamic Reference Tracking Experiment: To test the set-point tracking ability of the closed-loop WPT system, a cycling reference signal series is designed as

$$V_{ref}(k) = 60 \xrightarrow{T_4} 80 \xrightarrow{T_4} 100 \xrightarrow{T_4} 60 \cdots \tag{67}$$

where the switching time T_4 is set to 300 ms. The experimental result is shown in Fig. 13. Fig. 14 depicts the corresponding control actions of the MPC controller with constraints: $0 \le u(k) \le 100, k = 1, 2, \ldots, N_c$. From Fig. 13, it can be seen that the transient process can be finished within 20 ms and the closed-loop system has no overshoot nor undershoot. Hence, the MPC controller has good ability for dynamic reference tracking. Besides, it can be seen from Fig. 14 that all the control actions are limited to the preset range [0 V, 100 V].

2) Load Perturbation Experiment: Set the load to be changed suddenly from 10 to 20 Ω (Rate of change: 100%), and then from 20 to 30 Ω (Rate of change: 50%), respectively, with the reference voltage always being 100 V. The experimental results under load variation are shown in Fig. 15. It can be seen that the MPC controller provides satisfactory robustness against large load variation (Rate of change $\ge 50\%$). The settling time is very small and negligible. The overshoot and the undershoot remain 0%.

3) Water Flow Disturbance Experiment: In seawater environment, the seawater medium between power coils is not static and always moving, which may cause the variations of the conductivity and other unknown disturbances. To test the stability of the MPC control system in moving seawater medium, the water flow disturbance experiment is presented in this article. A water spiral is made near the coupler to produce persistent water flow

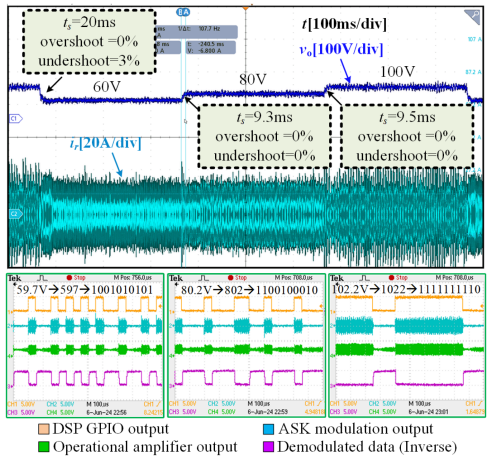

Fig. 13. Dynamic reference tracking process of MPC controller.

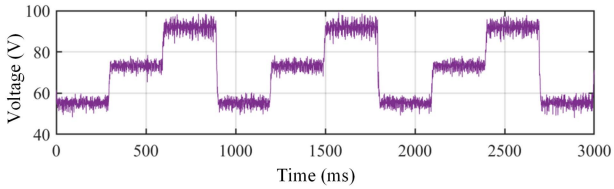

Fig. 14. Control actions of the MPC controller.

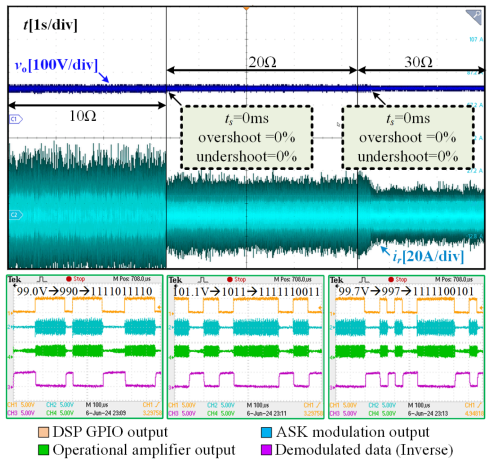

Fig. 15. Load perturbation experiment of MPC controller.

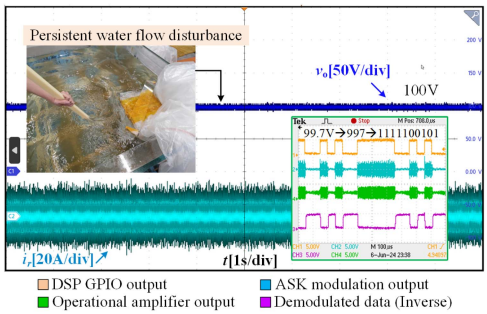

Fig. 16. Water flow disturbance experiment of MPC controller.

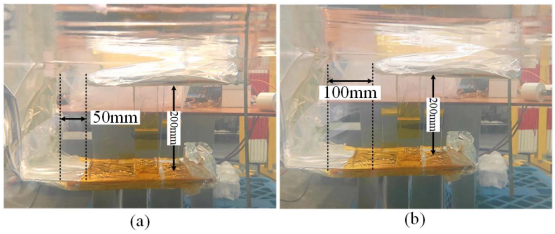

Fig. 17. Coil misalignment under different horizontal distances. (a) Horizontal misalignment of 50 mm. (b) Horizontal misalignment of 100 mm.

disturbance. It can be seen from Fig. 16 that the output of the closed-loop system is maintained to 100 V under the water flow disturbance.

4) Horizontal Misalignment Tolerance Experiment: During the operation of the WPT system in undersea applications, the positions of the coils may be perturbed due to the moving ocean current and other uncertain factors from the seawater environment. As coil misalignment happens, the transfer power of the WPT system may suffer much loss. Therefore, the horizontal misalignment tolerance experiment is designed to test the output stability of the closed-loop system in seawater environment. Fig. 17 shows the coil misalignment under different horizontal distances. The reference voltage is set as 60 V. The experimental result is shown in Fig. 18. It can be seen that with the regulation of the MPC controller, the output voltage of the WPT system can keep stable under the horizontal misalignment of [0 mm, 100 mm]. As the misalignment occurs, the controller adjusts the phase-shift angle of the inverter to adapt to the new operation condition.

Remark 5: The multiple peaks that occur on the control actions (see Fig. 14) may be caused by the measurement noise. As for the source of the measurement noise, it may be the EMI from other circuit modules, the peaks caused by the hard switch of the fixed-frequency inverter (see Fig. 18) or may be from the environment. The proposed MPC algorithm does not consider the influence of the noise, so as the noise enters into the control loop, the output $u(k)$ of the MPC controller may be accompanied by noise and induce disturbances in internal states (see i_r of Fig. 13). For perfect noise rejections, a pair of I/O filters will be considered to be added into the control algorithm in the future work.

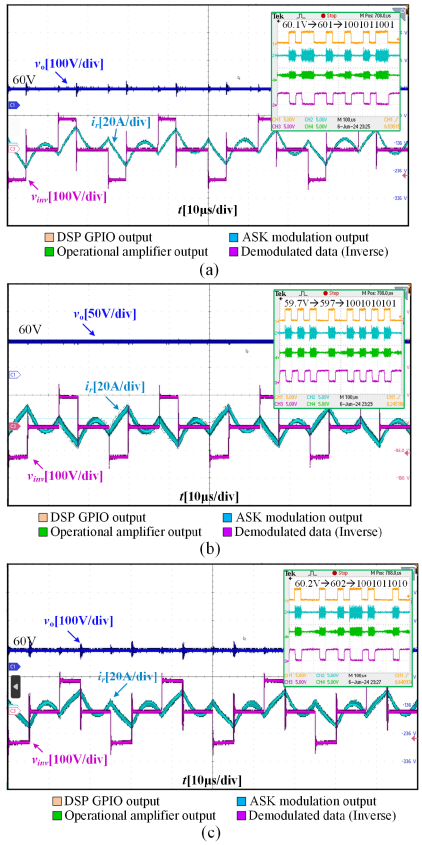

Fig. 18. Steady-state response of the closed-loop WPT system under different horizontal misalignment. (a) No misalignment. (b) Horizontal misalignment of 50 mm. (c) Horizontal misalignment of 100 mm.

D. Pole-Assignment-Based (PAB) PI Control

In addition, to further verify the advantage and superiority of the control performance of the proposed MPC controller, a PI controller based on the data-driven model is figured out. For fair comparison, the PI control system uses the MPC closed-loop dominant poles.

The closed-loop system is obtained by substituting (65) into the augmented system equation (36)

$$x(k+1) = (A - BK_{\text{mpc}})x(k) + BK_y V_{\text{ref}}(k). \tag{68}$$

The closed-loop eigenvalues can be evaluated through the closed-loop characteristic equation

$$\det[\lambda I - (A - BK_{\text{mpc}})] = 0. \tag{69}$$

Fig. 19 shows the $z-$plane pole distributions of the MPC-closed-loop WPT system.

In $z-$plane, the pole that is the nearest to the unit circle dominates the closed-loop system performance. Hence, the poles $\lambda_1 = 0.6748$ and $\lambda_2 = 0.9629$ are chosen as the dominant poles. Consider the relationship between $z-$ and $s-$plane variables

$$z = e^{T_s s} \Leftrightarrow s = \frac{\ln z}{T_s} \tag{70}$$

where T_s is the sampling interval.

The corresponding $s-$plane dominant poles are $s_1 = -393.4$ and $s_2 = -37.7846$. The first-order continuous transfer function

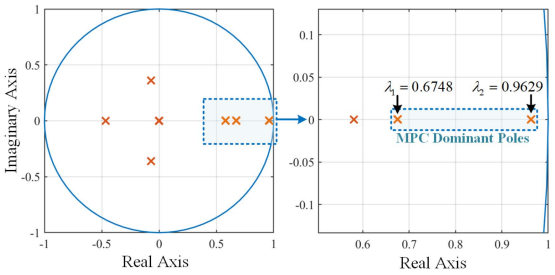

Fig. 19. $z-$plane pole distributions of the MPC-closed-loop WPT system.

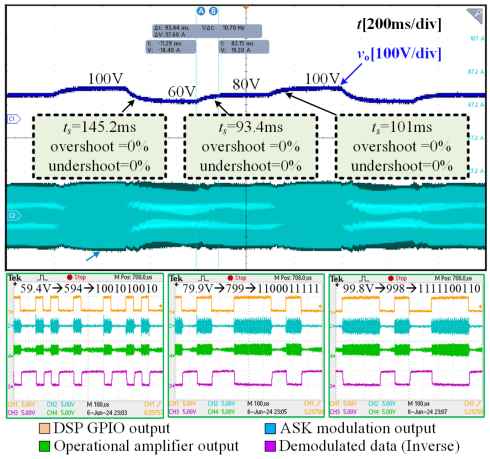

Fig. 20. Dynamic Reference tracking process of PAB-PI controller.

of the WPT system can be produced as

$$G_1(s) = \frac{742.5}{s + 696}. \tag{71}$$

The PI controller has the form as

$$K_{PI}(s) = K_p + K_i \frac{1}{s}. \tag{72}$$

The characteristic function of the PI control system is

$$f_{\text{PI}}(s) = 1 + G_1(s)K_{\text{PI}}(s) = 0. \tag{73}$$

Making the PI control system has the same poles with s_1 and s_2, the parameters of the PAB PI controller can be determined as $K_p = -0.3567$ and $K_i = 20.0195$.

1) Dynamic Reference Tracking Experiment: The reference signal for the test is selected as (67) shows. The experimental result is shown in Fig. 20. Seen from the results, as the reference voltage changes from 100 to 60 V, the closed-loop WPT system takes 145.2 ms to reach the steady state with no overshoot nor undershoot. As the reference voltage changes from 60 to 80 V and 80 to 100 V successively, the settling time of the PAB-PI controller are 93.4 and 101 ms, respectively. As it presents in Figs. 13 and 20, the PAB-PI controller can finally track the periodic reference signal, however the settling time is much longer compared to the MPC controller.

2) Load Perturbation Experiment: Along the same light of the MPC experiment, set the load to be changed between 10 and 30 Ω. The experimental results under load variation are shown in Fig. 21. It can be seen that as the load changes, the closed-loop WPT system can finally recover 100 V within 67 ms

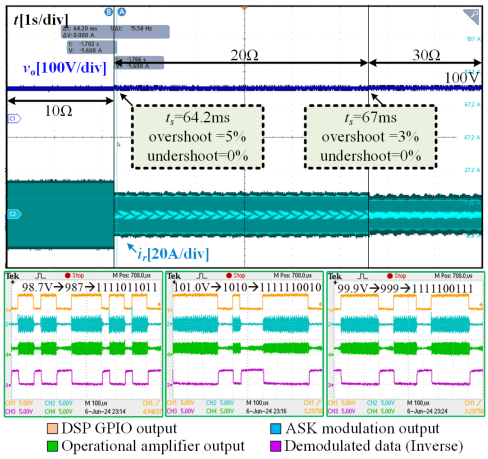

Fig. 21. Load perturbation experiment of PAB-PI controller. (a)R_L from 20 to 10 Ω. (b) R_L from 10 to 20 Ω.

TABLE III
COMPARISON BETWEEN THE MPC AND THE PI CONTROL

	PAB-PI	Observer-free MPC
Type of the controller	1DoF controller	2DoF controller
Settling time as reference changes	[93.4 ms,145.2 ms]	[9.3 ms,20 ms]
Recovering time as load varies	[64.2 ms,67 ms]	close to 0 ms
Overshoot	[0%,5%]	close to 0%
Undershoot	close to 0%	[0%,3%]

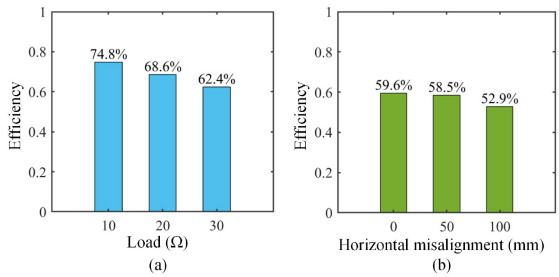

Fig. 22. System efficiency. (a) Efficiency under different loads. (b) Efficiency under different horizontal misalignment distances.

with maximum overshoot of 5%. It can be noted from Figs. 15 and 21 that the proposed MPC exhibits a much better robust performance compared to the PAB-PI control. The detailed performance difference between the PAB-PI and the observer-free MPC are shown in Table III.

E. Efficiency of the Closed-Loop System

The transmission efficiency of the closed-loop LCC-S compensated WPT system is investigated under different reference voltages, loads and horizontal misalignment distances. The calculation of the efficiency uses the readings of the dc power supply and the electronic load. As Fig. 22 demonstrates, as the load and the horizontal misalignment increase, the transmission efficiency of the WPT system decreases. Since the ECL caused

TABLE IV
COMPONENT PARAMETERS

Parameters	Values
Equivalent ON-state resistance of MOSFET r_{DS}	21 mΩ
Turn ON energy losses of MOSFET $e_{\text{SW-ON}}$	0.69 mJ
Turn OFF energy losses of MOSFET $e_{\text{SW-OFF}}$	0.42 mJ
Drain-source voltage of MOSFET V_R	1200 V
Drain-source current of MOSFET I_R	100 A
Reverse recovery charge of diode Q_{RR}	928 nC
Reference current of diode I_{R-D}	42 A
Threshold voltage of diode V_f	4.6 V
Equivalent ON-state resistance of diode r_D	51.1 mΩ
Equivalent resistance of seawater medium R_{sea1}	80 mΩ
Equivalent resistance of seawater medium R_{sea2}	81 mΩ
ESR of the transmitting coil R_1	80 mΩ
ESR of the receiving coil R_2	76 mΩ
ESR of the compensation inductor R_r	17 mΩ
Forward voltage of diode (rectifier) V_{f1}	1.4 V
Equivalent ON-state resistance of diode (rectifier) R_{D1}	46.7 mΩ

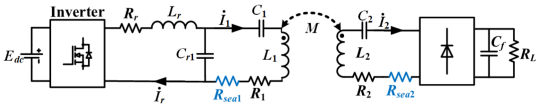

Fig. 23. Equivalent topology of the undersea LCC-S compensated WPT system.

by the highly conductive seawater exists, the overall efficiency of the WPT system is not beyond 75%.

VI. POWER LOSS ANALYSIS

For simplifying the analysis of the power losses of the seawater medium, an equivalent topology of the proposed *LCC*-S compensated WPT system is proposed in Fig. 23, where the influences from the seawater are simply assumed as the equivalent resistances R_{sea1} and R_{sea2} on the resonant tank. $\{R_r, R_1, R_2\}$ are the equivalent series resistances (ESRs) of the corresponding inductors. $\{\dot{I}_r, \dot{I}_1, \dot{I}_2\}$ are the phasor forms of the resonant currents.

The power losses of the proposed *LCC*-S compensated WPT system mainly consist of four parts, i.e., the losses of the inverters $P_{\text{inv-loss}}$, the seawater medium P_{SECL}, the resonant tank $P_{\text{ESR-loss}}$, and the rectifier $P_{\text{rec-loss}}$.

A. Power Losses of the Inverter

The power losses of the inverter mainly include MOSFETs conduction losses P_{mos}, switching losses P_{sw}, and antiparallel diodes losses P_{diode} [49].

1) Conduction Losses of MOSFETs:

$$P_{\text{mos}} = \frac{1}{\pi} r_{DS} I_r^2 (\pi + \alpha + \sin\alpha) \tag{74}$$

where r_{DS} is the equivalent onA-state resistance of MOSFET and α is the conduction angle of the inverter.

2) Switching Losses of MOSFETs and Diodes:

$$P_{\text{sw}} = 2\sqrt{2} f E_{\text{dc}} I_r \cos\left(\frac{\alpha}{2}\right)\left(\frac{e_{\text{SW-ON}} + e_{\text{SW-OFF}}}{V_R I_R} + \frac{Q_{RR}}{I_{R-D}}\right) \tag{75}$$

where $e_{\text{SW-ON}}$, $e_{\text{SW-OFF}}$, and V_R and I_R are the turn ON, turn OFF energy losses, and drain-source voltage, drain-source current of MOSFET, respectively. Q_{RR} and I_{R-D} are the reverse recovery charge and the reference current of the diode, respectively.

3) Conduction Losses of Diodes:

$$P_{\text{diode}} = \frac{2\sqrt{2}}{\pi} V_f I_r \left(1 - \sin\left(\frac{\alpha}{2}\right)\right) + \frac{1}{\pi} r_D I_r^2 (\pi - \alpha - \sin\alpha) \tag{76}$$

where V_f and r_D are the threshold voltage and the equivalent ON-state resistance of diode.

Therefore, the total power losses of the inverter can be given as follows:

$$P_{\text{inv-loss}} = P_{\text{mos}} + P_{\text{sw}} + P_{\text{diode}}. \tag{77}$$

B. Power Losses of the Seawater Medium

The seawater eddy current loss (SECL) is estimated via the following equation:

$$P_{\text{SECL}} = I_1^2 R_{\text{sea1}} + I_2^2 R_{\text{sea2}}. \tag{78}$$

The detection method of the equivalent resistance R_{sea1} and R_{sea2} can be described as follows: first, use the digital bridge to obtain the value of the ESR of the power coil, which is denoted as R_a. Second, put the coil into the water medium and use the digital bridge again to obtain the value of the ESR of the power coil, which is denoted as R_b. The value of the seawater equivalent resistance can be estimated as $R_{\text{sea}} = R_a - R_b$.

C. Power Losses of the Resonant Tank

The power losses of the resonant tank can be expressed as

$$P_{\text{ESR-loss}} = I_r^2 R_r + I_1^2 R_1 + I_2^2 R_2. \tag{79}$$

D. Power Losses of the Rectifier

$$P_{\text{Rec-loss}} = \frac{4\sqrt{2}}{\pi} V_{f1} I_2 + 2 I_2^2 R_{D1} \tag{80}$$

where V_{f1} and R_{D1} are the forward voltage and the equivalent ON-state resistance of the diodes in the rectifier.

The type of the MOSFET is C3M0021120K and the type of the rectifier diode is IDWD30G120C5. Related parameter values for loss analysis are given in Table IV. Letting l_h denote the horizontal misalignment distance, six operating conditions are studied to analyze the power loss distributions of the LCC-S compensated WPT system: 1) $R_L = 10\ \Omega, V_{\text{ref}} = 100\ \text{V}, l_h = 0$ mm. 2) $R_L = 20\ \Omega, V_{\text{ref}} = 100\ \text{V}, l_h = 0$ mm. 3) $R_L = 30\ \Omega, V_{\text{ref}} = 100\ \text{V}, l_h = 0$ mm. 4) $R_L = 30\ \Omega, V_{\text{ref}} = 60\ \text{V}, l_h = 0$ mm. 5) $R_L = 30\ \Omega, V_{\text{ref}} = 60\ \text{V}, l_h = 50$ mm. 6) $R_L = 30\ \Omega, V_{\text{ref}} = 60\ \text{V}, l_h = 100$ mm.

The results are shown in Fig. 24. Based on the actual measured I_r, I_1, and I_2, combined with the selected MOSFETs and Schottky diodes parameters, as well as the ESRs of the resonant tank and the seawater equivalent resistance, the detailed losses of the inverter, seawater medium, resonant tank, and rectifier can be calculated from (74) to (80). It can be seen that the SECL is very close to the ESR loss, which contributes the most to the overall power loss, followed by the inverter and rectifier losses. When the load resistance R_L increases and the reference voltage keeps

TABLE V
COMPARISON WITH EXISTING CONTROL METHODS FOR WPT SYSTEMS IN SEAWATER ENVIRONMENT

	This work	[23]	[24]	[25]
Control objective	**Output voltage**	Output voltage	Output voltage Output current	Output current
Control techniques	**Observer-free MPC**	NVOCC	PI-DCC	PI control
Actuator of control actions	**Primary-side inverter**	Secondary-side converter	Secondary-side converter	Variable Inductor
Wireless communication	**Yes**	No	No	No
Additional regulation circuit	**No**	Switched capacitor converter	Buck converter	A single variable inductor
Validation platform	**Real prototype**	Virtual simulation	Virtual simulation	Real prototype
Transmission distance	**20cm**	Not mentioned	Not mentioned	[0cm,14cm]
Settling time	**[0ms,20ms]**	0ms	[0.4ms,1.5ms]	Not mentioned
Overshoot	**0%**	0%	[0%,46%]	Not mentioned
Undershoot	**[0%,3%]**	0%	[0%,33%]	Not mentioned
Conductivity of the seawater	**4.9S/m**	Not mentioned	Not mentioned	3S/m
Maximum output power	**1kW**	20W	96W	1kW
Maximum efficiency	**74.8%**	Not mentioned	77%	96.1%
Computational Resources	**18 times of $\pm$ operations** **10 times of $\times$ operations** **2 times of assignment operations** **2 times of comparing operations**	2 times of $\pm$ operations 3 times of $\times$ operations	11 times of $\pm$ operations 9 times of $\times$ operations	4 times of $\pm$ operations 3 times of $\times$ operations 1 time of saturation operation

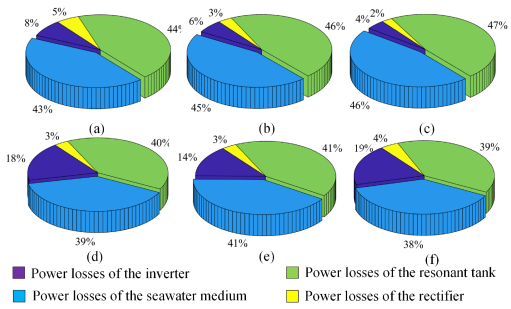

Fig. 24. Power loss distributions. (a) $R_L = 10\ \Omega, V_{\text{ref}} = 100$ V, $l_h = 0$ mm. (b) $R_L = 20\ \Omega, V_{\text{ref}} = 100$ V, $l_h = 0$ mm. (c) $R_L = 30\ \Omega, V_{\text{ref}} = 100$ V, $l_h = 0$ mm. (d) $R_L = 30\ \Omega, V_{\text{ref}} = 60$ V, $l_h = 0$ mm. (e) $R_L = 30\ \Omega, V_{\text{ref}} = 60$ V, $l_h = 50$ mm. (f) $R_L = 30\ \Omega, V_{\text{ref}} = 60$ V, $l_h = 100$ mm.

invariant, I_r, I_1 and I_2 all decreases, which leads to the decrease of the inverter and rectifier losses. As a result, the ratio of the SECL increases slightly. When the horizontal misalignment increases, to maintain the output voltage, the amplitudes of the resonant tank currents will be regulated to adapts to the new operating condition. For all cases, the SECL and ESR losses dominate the overall power losses.

VII. COMPARISON AND DISCUSSION

A comparative study with different control techniques for the wireless charging system in undersea conditions is given in Table V. Specogna et al. [1] proposed a NVOCC method to regulate the output voltage of the undersea WPT system. This method uses the single-bridge switched capacitor converter to replace the traditional full-bridge rectifier, which decreases the circuit complexity. The dynamic response speed under parameter perturbation is close to 0 ms. However, the output power under NVOCC method is only 20 W and the information of the seawater conductivity and transfer distance is not provided. Dai et al. [2] proposed a PI-DCC method to realize multi-variable control. Although it has a quick convergency speed within 1.5 ms, it needs an extra buck converter in the secondary side. Besides, it has considerable overshoot (46%) and undershoot (33%) during the regulation process. Li et al. [3] utilizes a single variable inductor as the actuator of the PI controller to achieve output current control of the undersea WPT systems. A high output power of 1 kW with efficiency of 96.1% is reached using this method. But the dynamic response information is not provided. Besides, the transfer distance is within 14 cm and the conductivity is only 3 S/m, which indicates a milder seawater environment than that in our work. Compared to these methods, the proposed observer-free MPC method takes advantages of the SRIV data-driven modeling algorithm to cover the unknown dynamics from the seawater environment with conductivity of 4.9 S/m, and utilizes the receding optimization nature of the MPC algorithm. Thus, the great dynamic response quality and parametric robustness are both achieved under the highly conductive medium.

VIII. CONCLUSION

When it comes to the control design of the WPT system, the dynamic modeling of it should be considered first. Since the power transfer medium is the seawater, the dynamics is much different from the condition in air. For accurately describing the dynamics of the WPT system, the SRIV method is adopted to model the WPT system, which only uses the I/O data of it to form an OE model. Then, a NMSS model is constructed based on the OE model and then augmented by inserting an action of an integrator for the observer-free MPC design. Considering the limits on the control input, the Hildreth's procedure is introduced to calculate the control action. The effectiveness of the proposed control scheme has been tested on a LCC-S compensated WPT system. It is illustrated through several results that the proposed data-driven-model-based MPC achieves an excellent dynamic closed-loop performance. Furthermore, the proposed MPC strategy can be easily expanded to the transcutaneous biomedical applications of WPT systems.

REFERENCES

[1] R. Specogna et al., "Detailed circuit modelling of phone charging wireless power transfer," in *2021 IEEE Appl. Power Electron. Conf. Expo.*, 2021, pp. 463–467.

[2] X. Dai, J.-C. Jiang, and J.-Q. Wu, "Charging area determining and power enhancement method for multiexcitation unit configuration of wirelessly dynamic charging EV system," *IEEE Trans. Ind. Electron.*, vol. 66, no. 5, pp. 4086–4096, May 2019.

[3] Y. Li et al., "A new coil structure and its optimization design with constant output voltage and constant output current for electric vehicle dynamic wireless charging," *IEEE Trans. Ind. Informat.*, vol. 15, no. 9, pp. 5244–5256, Sep. 2019.

[4] M. McDonough, "Integration of inductively coupled power transfer and hybrid energy storage system: A multiport power electronics interface for battery-powered electric vehicles," *IEEE Trans. Power Electron.*, vol. 30, no. 11, pp. 6423–6433, Nov. 2015.

[5] T. M. Hayslett, T. Orekan, and P. Zhang, "Underwater wireless power transfer for ocean system applications," in *Proc. OCEANS 2016 MTS/IEEE Monterey*, 2016, pp. 1–6.

[6] R. S. McEwen, B. W. Hobson, L. McBride, and J. G. Bellingham, "Docking control system for a 54-cm-diameter (21-in) AUV," *IEEE J. Ocean. Eng.*, vol. 33, no. 4, pp. 550–562, Oct. 2008.

[7] R. Stokey et al., "Enabling technologies for REMUS docking: An integral component of an autonomous ocean-sampling network," *IEEE J. Ocean. Eng.*, vol. 26, no. 4, pp. 487–497, Oct. 2001.

[8] K. Teo, E. An, and P.-P. J. Beaujean, "A robust fuzzy autonomous underwater vehicle (AUV) docking approach for unknown current disturbances," *IEEE J. Ocean. Eng.*, vol. 37, no. 2, pp. 143–155, Apr. 2012.

[9] T. Orekan, P. Zhang, and C. Shih, "Analysis, design, and maximum power-efficiency tracking for undersea wireless power transfer," *IEEE J. Emerg. Sel. Topics Power Electron.*, vol. 6, no. 2, pp. 843–854, Jun. 2018.

[10] R.-F. Xue, K.-W. Cheng, and M. Je, "High-efficiency wireless power transfer for biomedical implants by optimal resonant load transformation," *IEEE Trans. Circuits Syst. I, Reg. Papers*, vol. 60, no. 4, pp. 867–874, Apr. 2013.

[11] D. Ahn and S. Hong, "Wireless power transmission with self-regulated output voltage for biomedical implant," *IEEE Trans. Ind. Electron.*, vol. 61, no. 5, pp. 2225–2235, May 2014.

[12] S. Stoecklin, A. Yousaf, T. Volk, and L. Reindl, "Efficient wireless powering of biomedical sensor systems for multichannel brain implants," *IEEE Trans. Instrum. Meas.*, vol. 65, no. 4, pp. 754–764, Apr. 2016.

[13] J. Zhou, D. J. Li, and Y. Chen, "Frequency selection of an inductive contactless power transmission system for ocean observing," *Ocean Eng.*, vol. 60, pp. 175–185, 2013.

[14] J. Kim, K. Kim, H. Kim, D. Kim, J. Park, and S. Ahn, "An efficient modeling for underwater wireless power transfer using Z-parameters," *IEEE Trans. Electromagn. Compat.*, vol. 61, no. 6, pp. 2006–2014, Dec. 2019.

[15] Z. Yan et al., "Frequency optimization of a loosely coupled underwater wireless power transfer system considering eddy current loss," *IEEE Trans. Ind. Electron.*, vol. 66, no. 5, pp. 3468–3476, May 2019.

[16] K. Zhang, Y. Ma, Z. Yan, Z. Di, B. Song, and A. P. Hu, "Eddy current loss and detuning effect of seawater on wireless power transfer," *IEEE J. Emerg. Sel. Topics Power Electron.*, vol. 8, no. 1, pp. 909–917, Mar. 2020.

[17] N. Soltani, M. ElAnsary, J. Xu, J. S. Filho, and R. Genov, "Safety-optimized inductive powering of implantable medical devices: Tutorial and comprehensive design guide," *IEEE Trans. Biomed. Circuits Syst.*, vol. 15, no. 6, pp. 1354–1367, Dec. 2021.

[18] K. van Oosterhout, M. Paulides, H. Pflug, S. Beumer, and R. Mestrom, "An approximate electromagnetic model for optimizing wireless charging of biomedical implants," *IEEE Trans. Biomed. Eng.*, vol. 69, no. 6, pp. 1954–1963, Jun. 2022.

[19] Y.-L. Li, Y. Sun, and X. Dai, "Robust control for an uncertain LCL resonant ICPT system using LMI method," *Control Eng. Pract.*, vol. 21, no. 1, pp. 31–41, 2013.

[20] C. Xia, W. Wang, S. Ren, X. Wu, and Y. Sun, "Robust control for inductively coupled power transfer systems with coil misalignment," *IEEE Trans. Power Electron.*, vol. 33, no. 9, pp. 8110–8122, Sep. 2018.

[21] Y. Liang et al., "H∞ robust control for ICPT system with selected weighting function considering parameter perturbations," *IEEE Trans. Power Electron.*, vol. 37, no. 11, pp. 13914–13929, Nov. 2022.

[22] Z. Yu, Y. Sun, X. Dai, and Z. Ye, "Stability and control of uncertain ICPT system considering time-varying delay and stochastic disturbance," *Int. J. Robust Nonlinear Control*, vol. 29, no. 18, pp. 6582–6604, 2019.

[23] L. Yang, B. Zhang, and M. Ju, "A fast dynamic response regulation method for undersea wireless power transfer system," in *2019 14th IEEE Conf. Ind. Electron. Appl.*, 2019, pp. 1162–1166.

[24] Z. Zheng, N. Wang, and S. Ahmed, "Decoupling control scheme bridging frequency tracking and DC output stabilizing for wireless charging system of autonomous underwater vehicles," *Int. J. Control Autom. Syst.*, vol. 20, pp. 1099–1110, 2022.

[25] J. Li, C. Zhu, J. Xie, F. Lu, and X. Zhang, "Design and implementation of high-misalignment tolerance WPT system for underwater vehicles based on a variable inductor," *IEEE Trans. Power Electron.*, vol. 38, no. 10, pp. 11726–11737, Oct. 2023.

[26] F. Chen, H. Garnier, Q. Deng, M. K. Kazimierczuk, and X. Zhuan, "Control-oriented modeling of wireless power transfer systems with phase-shift control," *IEEE Trans. Power Electron.*, vol. 35, no. 2, pp. 2119–2134, Feb. 2020.

[27] F. Chen, P. C. Young, H. Garnier, Q. Deng, and M. K. Kazimierczuk, "Data-driven modeling of wireless power transfer systems with multiple transmitters," *IEEE Trans. Power Electron.*, vol. 35, no. 11, pp. 11363–11379, Nov. 2020.

[28] F. Chen, A. Padilla, P. C. Young, and H. Garnier, "Data-driven modeling of wireless power transfer systems with slowly time-varying parameters," *IEEE Trans. Power Electron.*, vol. 35, no. 11, pp. 12442–12456, Nov. 2020.

[29] F. Chen, Z. Deng, H. Hu, and Y. Sun, "Dynamic reduced-order modeling of wireless power transfer systems via polynomial approximation," *IEEE Trans. Power Electron.*, vol. 37, no. 7, pp. 7540–7547, Jul. 2022.

[30] J. Tang, S. Dong, C. Cui, and Q. Zhang, "Sampled-data modeling for wireless power transfer systems," *IEEE Trans. Power Electron.*, vol. 35, no. 3, pp. 3173–3182, Mar. 2020.

[31] B.-G. Choi and Y.-S. Kim, "New structure design of ferrite cores for wireless electric vehicle charging by machine learning," *IEEE Trans. Ind. Electron.*, vol. 68, no. 12, pp. 12162–12172, Dec. 2021.

[32] M. S. Jeong, J. H. Jang, and E. S. Lee, "Optimal IPT core design for wireless electric vehicles by reinforcement learning," *IEEE Trans. Power Electron.*, vol. 38, no. 11, pp. 13262–13272, Nov. 2023.

[33] Y. Xie, R. Ghaemi, J. Sun, and J. S. Freudenberg, "Implicit model predictive control of a full bridge DC-DC converter," *IEEE Trans. Power Electron.*, vol. 24, no. 12, pp. 2704–2713, Dec. 2009.

[34] Y. Bak, Y. J. Lee, and K.-B. Lee, "Dynamic characteristic improvement of phase-shift full-bridge center-tapped converters using a model predictive control," *IEEE Trans. Ind. Electron.*, vol. 69, no. 2, pp. 1488–1497, Feb. 2022.

[35] J. Saeed, L. Wang, and N. Fernando, "Model predictive control of phase shift full-bridge DC-DC converter using Laguerre functions," *IEEE Trans. Control Syst. Technol.*, vol. 30, no. 2, pp. 819–826, Mar. 2022.

[36] Z. Zhou, L. Zhang, Z. Liu, Q. Chen, R. Long, and H. Su, "Model predictive control for the receiving-side DC-DC converter of dynamic wireless power transfer," *IEEE Trans. Power Electron.*, vol. 35, no. 9, pp. 8985–8997, Sep. 2020.

[37] C. Qi, Z. Lang, L. Su, X. Chen, and H. Miao, "Model predictive control for a bidirectional wireless power transfer system with maximum efficiency point tracking," in *Proc. IEEE Int. Symp. Predictive Control Elect. Drives Power Electron.*, 2019, pp. 1–5.

[38] C. Qi, Z. Lang, L. Su, X. Chen, and H. Miao, "Finite-control-set model predictive control for a wireless power transfer system," in *2019 IEEE Int. Symp. Predictive Control Elect. Drives Power Electron.*, 2019, pp. 1–5.

[39] S. Liu et al., "Dynamic improvement of inductive power transfer systems with maximum energy efficiency tracking using model predictive control: Analysis and experimental verification," *IEEE Trans. Power Electron.*, vol. 35, no. 12, pp. 12752–12764, Dec. 2020.

[40] S. Chen, W. Ding, L. Huo, X. Wu, S. Shi, and R. Hu, "Dynamic improvement and efficiency optimization of wireless power transfer systems using improved FCS-MPC and P&O methods," *IEEE Trans. Power Electron.*, vol. 38, no. 11, pp. 14702–14718, Nov. 2023.

[41] D. Mayne, J. Rawlings, C. Rao, and P. Scokaert, "Constrained model predictive control: Stability and optimality," *Automatica*, vol. 36, no. 6, pp. 789–814, 2000.

[42] Y. Li, R. Mai, L. Lu, and Z. He, "Active and reactive currents decomposition-based control of angle and magnitude of current for a parallel multiinverter IPT system," *IEEE Trans. Power Electron.*, vol. 32, no. 2, pp. 1602–1614, Feb. 2017.

[43] P. C. Young, *Recursive Estimation and Time-Series Analysis*. Berlin, Germany: Springer, 2011.

[44] L. Wang and P. C. Young, "An improved structure for model predictive control using non-minimal state space realisation," *J. Process Control*, vol. 16, no. 4, pp. 355–371, 2006.

[45] L. Wang, *Model Predictive Control System Design and Implementation Using Matlab*. Berlin, Germany: Springer, 2009.
[46] C. Hildreth, "A quadratic programming procedure," *Nav. Res. Logistics Quart.*, vol. 4, no. 1, pp. 79–85, 1957.
[47] C. Da, L. Wang, F. Li, C. Tao, and Y. Zhang, "Analysis of undersea simultaneous wireless power and 1 Mb/s data rate transfer system based on DDQ coil," *IEEE Trans. Power Electron.*, vol. 38, no. 10, pp. 11814–11825, Oct. 2023.
[48] X. Li, j. Hu, Y. Li, H. Wang, M. Liu, and P. Deng, "A decoupled power and data-parallel transmission method with four-quadrant misalignment tolerance for wireless power transfer systems," *IEEE Trans. Power Electron.*, vol. 34, no. 12, pp. 11531–11535, Dec. 2019.
[49] Y. Li et al., "Efficiency analysis and optimization control for input-parallel output-series wireless power transfer systems," *IEEE Trans. Power Electron.*, vol. 35, no. 1, pp. 1074–1085, Jan. 2020.

Ziyi Xia (Student Member, IEEE) received the B.S. degree in automation from the Nanjing University of Aeronautics and Astronautics, Nanjing, China, in 2016, and the M.S. degree in control science and engineering in 2021 from Chongqing University, Chongqing, China, where he is currently working toward the Ph.D. degree in control science and engineering.

His research interests include wireless power transfer systems, model predictive control, robust control, and data-driven control.

Xin Dai (Member, IEEE) received the B.S. degree in industrial automation from Yuzhou University, Chongqing, China, in 2000, and the Ph.D. degree in control theory and control engineering from the School of Automation, Chongqing University, Chongqing, China, in 2006.

In 2012, he was a Visiting Scholar with The University of Auckland, Auckland, New Zealand. He is currently working as a Professor with the School of Automation, Chongqing University. His research interests include inductive power transfer technology and nonlinear dynamic behavior analysis of power electronics.

Yanling Li received the Ph.D. degree in control theory and control engineering from the School of Automation, Chongqing University, Chongqing, China, in 2017.

She is currently working with the School of Electrical Engineering and Electronics Information, Xihua University, Chengdu, China. Her research interests include wireless power transfer and advanced control technology in power electronics.

Liuping Wang (Senior Member, IEEE) received the Ph.D. degree in automatic control and systems engineering from the Department of Automatic Control and Systems Engineering, University of Sheffield, Sheffield, U.K., in 1989.

Upon completion of her Ph.D. degree, she worked with the Department of Chemical Engineering, University of Toronto, Toronto, ON, Canada, for eight years in the field of process control. From 1998 to 2002, she worked with the Center for Integrated Dynamics and Control, Callaghan, NSW, University of Newcastle, Australia. In 2002, she joined the School of Electrical and Computer Engineering, RMIT University, Melbourne, VIC, Australia where she is a Professor of Control Engineering since 2007. She has authored and coauthored more than 300 scientific papers in the field of system identification, PID control, adaptive control, model predictive control, electrical drive control and control technology application to industrial processes. She is the author or a lead author of the following five books: *Model Predictive Control Design and Implementation* using MATLAB (Springer, 2009); *PID control system design and automatic tuning* using MATLAB/Simulink (Wiley-IEEE Press, 2020); *State feeddback control and Kalman filtering* with MATLAB/Simulink tutorials (Wiley-IEEE Press, 2022); *PID and predictive control of electrical drives and power converters* using MATLAB (Wiley-IEEE Press, 2015) and *From process data to process control- ideas for process identification and PID control* (Taylor and Francis, 2000). Two of her recent books have been translated into Chinese and published by Tsinghua University Press (2023) and China Science Press (2024).

Fengwei Chen (Member, IEEE) was born in Chongqing, China. He received the B.Eng. degree in automation and the M.Eng. degree in control theory and control engineering from Wuhan University, Wuhan, China, in 2009 and 2011, respectively, and the Ph.D. degree in automatic control from the Université de Lorraine, Nancy, France, in 2014.

From 2015 to 2016, he was a Lecturer with the Dalian University of Technology, Dalian, China. From 2017 to 2020, he was an Associate Researcher with Wuhan University. Since 2021, he has been an Associate Professor with Chongqing University, Chongqing, China. His research interests include system identification and parameter estimation, with applications to wireless power transfer.

Wei Wang (Student Member, IEEE) received the B.E. degree in automation in 2021 from the College of Automation, Chongqing University, Chongqing, China, where he is currently working toward the master degree in electronic information engineering.

His research interests include modeling and control technology for wireless power transfer.